

# An Upwind Generalized Finite Difference Method (GFDM) for Analysis of Heat and Mass Transfer in Porous Media

Xiang Rao, Hui Zhao, Zhan Wentao

School of Petroleum Engineering, Yangtze University, Wuhan, China

## Abstract

In this paper, an upwind meshless GFDM is presented for the first time and applied to the coupled computation of heat and mass transfer in porous media. The GFDM based sequential coupled discrete schemes of the pressure diffusion equation and thermal convection-diffusion equation, the upwind scheme of physical parameters without modifying node influence domain and the treatment of heterogeneous physical parameters in GFDM are given. Three numerical examples illustrate the good computational performances of the presented upwind GFDM and the application of the method to numerical solutions of the convection-diffusion equation. This study shows that this upwind GFDM, which can flexibly characterize the computational domain through allocation nodes without complicated mesh division and has sufficient accuracy, may have great potential to be developed as a general numerical simulator in the multi-physics coupling problem with complex geometry.

**Keywords:** generalized finite difference method; meshless method; heat and mass transfer; upwind scheme; multi-physics coupling problem;

## 1. Introduction

The study on heat and mass transfer in porous media widely exists in the development and utilization of environment-friendly geothermal resources, thermal recovery of oil and gas resources, thermal performance of insulation materials, etc. Underground reservoir rocks are typical porous media, among which the study on coupled heat and mass transfer focuses on the coupling calculation of fluid seepage and heat conduction-convection in porous formation. This coupling effect is mainly reflected in the following aspects [1]: (1) the influence of temperature change on fluid viscosity; (2) the influence of temperature on formation porosity; (3) the influence of fluid flow velocity on the strength of heat convection, etc.; At present, the numerical simulation methods of coupled mass transfer and heat transfer mainly include finite difference method (FDM) [2], finite element method (FEM) [3], and finite volume method (FVM) [4,5]. However, these methods are limited by the requirements of geometric regularity of the computational domain and high-quality mesh generation.

Generalized finite difference method (GFDM) is a new type of domain-type meshless method developed in recent years. Based on Taylor series expansion of unknown function and weighted least square approximation in a subdomain, the partial derivatives of unknown function in the governing equation are expressed as the linear combination of function values of nodes in the subdomain, which overcomes the grid dependence of traditional FDM [6]. Benito et al. proposed an adaptive GFDM, which realized the local automatic collocation according to the accuracy requirements [7]. Up to now, GFDM has been widely used to solve various scientific and engineering problems, including coupled thermoelasticity problem [8-10], third and fourth-order partial differential equations [11], shallow water equations [12], transient heat conduction analysis [13], seismic wave propagation problem [14], stress analysis [15], unsteady Burgers' equations [16-17], water wave interactions [18], inverse heat source problems [19], nonlinear convection-diffusion equations [20], time-fractional diffusion equation [21], stochastic subsurface flow [22]. Gavete et al. [23] reviewed the advantages and disadvantages of GFDM and its applications, analyzed the influence of various factors on the numerical performances of GFDM, and found that the weight function has little influence on the numerical results. Therefore, in the practical application of GFDM, the quartic spline function is often used as the weight function. In general, the GFDM only needs to arrange a group of nodes in the computational domain to realize the accurate solution of the governing equation, which saves the time-consuming and laborious meshing and numerical integration in the finite element method, finite difference method, and boundary element method for the computational domain with complex geometry.

This paper focuses on applying GFDM to the modeling of coupled heat and mass transfer problem, which involves not only the diffusion equation about pressure, but also the heat convection-diffusion equation. For the convection-diffusion equation, it is often necessary to add upwind weight treatment to the discrete scheme of the convection term, otherwise, the calculation solution is prone to the situation of inaccurate oscillation. For example, the upstream FEM [24], the upstream FDM [25], and the upstream FVM [26] have been widely used. In the meshless method, currently, modifying the influence domain is generally adopted to realize the

upstream weight, including the upwind influence domain [27] of moving the central node position in the upstream direction and the partial influence domain [28] of including the upstream nodes more in the central-node influence domain. However, due to the fact that the actual flow field may be very complex, it is difficult to obtain a stable upwind effect by modifying the influence domain, and the calculation accuracy is difficult to be effectively guaranteed. For GFDM, Cheng and Liu [28] roughly discussed the upwind effect by constructing a six-point scheme containing more upstream nodes in the influence domain in GFDM, however, this method is limited to adopting a specific six-point format in the node distribution of almost orthogonal parts, and if the upstream conditions of different nodes in the flow field are different, then this method is difficult to obtain the stable upwind effect and high calculation accuracy and lacks good generalization.

Therefore, this paper aims at the effective meshless modeling of single-phase coupled heat and mass transfer based on GFDM, including the sequential coupled discrete scheme of partial differential equations about pressure and temperature based on GFDM, the upwind scheme of physical parameters without modifying the influence domain, and the treatment of heterogeneous physical parameters when the explicit function form of physical parameters is unknown. Then, an upwind GFDM method that can effectively solve the convection-diffusion equation is formed, in order to provide valuable reference and an useful tool for the application of GFDM in multi-physical field coupling modeling.

The paper is structured as follows. In Section 2, we introduce GFDM based modeling process of single-phase heat and mass transfer, including the basic physical model in Section 2.1, the basic principle of GFDM in Section 2.2, the upwind GFDM discrete schemes of mass and heat transfer equations in Section 2.3 and the treatment of boundary conditions in section 2.4. Section 3 gives three numerical examples to validate the upwind scheme and high computational accuracy of the presented method and discusses the application of upwind GFDM in the numerical solution of the convection-diffusion equation. The conclusion and future work come in Section 4.

## 2. Methodology

### 2.1 Physical model

This paper focuses on the study of single-phase heat and mass transfer in porous media, including flow equation about pressure, convection-diffusion equation about temperature, and auxiliary equations of physical quantities affected by pressure and temperature, which are:

(1) Mass conservative equation (Assuming that the fluid is incompressible)

$$0.0864\nabla \cdot \left( \frac{k}{\mu(T)} \nabla p \right) + q = \frac{\partial \phi(p, T)}{\partial t} \quad (1)$$

where  $k$  is absolute permeability, mD;  $t$  is time, day;  $\mu(T)$  is oil viscosity which is a function of temperature, mPa·s;  $p$  is pressure, MPa;  $q$  is the source or sink term, 1/day;  $\phi(p, T)$  is the porosity of underground formation which is a function of pressure and temperature, fraction. The unit of length is meter.

(2) Energy conservative equation

$$86400\nabla (\lambda_c(p, T) \nabla T) + 0.0864\nabla \left( \rho_l C_l T \frac{k}{\mu} \nabla p \right) + q_H = \frac{\partial}{\partial t} \left[ (1 - \phi(p, T)) \rho_r C_r T + \phi(p, T) \rho_l C_l T \right] \quad (2)$$

where  $T$  is temperature, °C;  $\lambda_c(p, T)$  is the integrated heat conduction coefficient which is the function of pressure and temperature, J/s/m/°C;  $C_l$  is the heat capacity of the fluid, J/kg/°C;  $\rho_r$  is rock density, kg/m<sup>3</sup>;  $C_r$  is the heat capacity of rock, J/kg/°C;  $q_H$  is the energy source or sink term corresponding to the total heat energy carried by the source or sink terms  $q$ , J/m<sup>3</sup>/day.

(3) Auxiliary equations

Due to the elastic and thermoelastic properties of reservoir porous media, porosity is affected by both fluid pressure and temperature. The expression is as follows:

$$\phi(p, T) = \left[ \phi_0 + C_i (p - p_0) \right] \left[ 1 + \frac{(1 - \phi_0)}{\phi_0} C_{Temp} (T - T_0) \right] \quad (3)$$

where  $C_i$  is the fluid compressibility coefficient, 1/MPa;  $C_{Temp}$  is the thermal expansion coefficient, 1/°C;  $p_0$  is the initial formation pressure, MPa;  $T_0$  is initial formation temperature, °C;  $\phi_0$  is the porosity when  $p_0$  and  $T_0$ .

The integrated heat conduction coefficient is expressed as

$$\lambda_c(p, T) = \phi(p, T)\lambda_l + (1 - \phi(p, T))\lambda_r \quad (4)$$

where  $\lambda_l$  and  $\lambda_r$  are heat conduction coefficients of fluid and rock, respectively.

$$\mu(T) = \mu(T_0)e^{-\alpha_T(T-T_0)} \quad (5)$$

where  $\alpha_T$  is the fluid viscosity-temperature coefficient, which represents the physical law that the fluid viscosity decreases with the increase of temperature.

It can be seen that, Eqs. (1) and (2) are differential equations about temperature and pressure, in which Eq. (1) is mainly pressure diffusion equation and Eq. (2) is mainly convection-diffusion equation about temperature, but the coefficient terms in these two equations will be jointly affected by pressure and temperature to form a nonlinear equation system.

## 2.2 A brief review of GFDM

GFDM is a relatively new meshless collocation method based on local Taylor expansion and moving least squares approximation. In this method, the partial derivation of unknown variables is approximated as a linear combination of node function values within each local subdomain.

There are  $n$  other nodes in the influence domain of the node  $M_0 = (x_0, y_0)$ , which are denoted as  $\{M_1, M_2, M_3, \dots, M_N\}$  where  $M_i = (x_i, y_i)$ . Taylor expansions of the field variable values  $\{u(M_i), i=1, \dots, n\}$  at node  $M_0$  are obtained:

$$u(M_i) = u(M_0) + \Delta x_i \left. \frac{\partial u}{\partial x} \right|_{M_0} + \Delta y_i \left. \frac{\partial u}{\partial y} \right|_{M_0} + \frac{1}{2} \left( (\Delta x_i)^2 \left. \frac{\partial^2 u}{\partial x^2} \right|_{M_0} + 2\Delta x_i \Delta y_i \left. \frac{\partial^2 u}{\partial x \partial y} \right|_{M_0} + (\Delta y_i)^2 \left. \frac{\partial^2 u}{\partial y^2} \right|_{M_0} \right) + o(r^3) \quad (6)$$

where  $\Delta x_i = x_0 - x_i$ ,  $\Delta y_i = y_0 - y_i$ .

$$\text{Denote } u_0 = u(M_0), \quad u_{x0} = \left. \frac{\partial u}{\partial x} \right|_{M_0}, \quad u_{y0} = \left. \frac{\partial u}{\partial y} \right|_{M_0}, \quad u_{xx0} = \left. \frac{\partial^2 u}{\partial x^2} \right|_{M_0}, \quad u_{xy} = \left. \frac{\partial^2 u}{\partial x \partial y} \right|_{M_0}, \quad u_{yy} = \left. \frac{\partial^2 u}{\partial y^2} \right|_{M_0}.$$

Define weighted error function  $B(\mathbf{D}_u)$ :

$$B(\mathbf{D}_u) = \sum_{j=1}^n \left[ \left( u_0 - u_j + \Delta x_j u_{x0} + \Delta y_j u_{y0} + \frac{1}{2} (\Delta x_j)^2 u_{xx0} + \frac{1}{2} (\Delta y_j)^2 u_{yy0} + \Delta x_j \Delta y_j u_{xy0} \right) \omega_j \right]^2 \quad (7)$$

where  $\mathbf{D}_u = (u_{x0}, u_{y0}, u_{xx0}, u_{yy0}, u_{xy0})^T$ ,  $\omega_j = \omega(\Delta x_j, \Delta y_j)$  is the weight function, Pan and Li [16] demonstrated that different types of weight function have little influence on the calculation results, while the quartic spline function is generally selected as the weight function in Eq. (8).

$$\omega_j = \begin{cases} 1 - 6 \left( \frac{r_j}{r_m} \right)^2 + 8 \left( \frac{r_j}{r_m} \right)^3 - 3 \left( \frac{r_j}{r_m} \right)^4 & r_j \leq r_m \\ 0 & r_j > r_m \end{cases} \quad (8)$$

where  $r_j$  is the Euclidean distance from the node  $M_j$  to the node  $M_0$ , and  $r_m$  is the radius of the influence domain of  $M_0$ .

To obtain the best estimate of the Laplacian operator, the error function  $B(\mathbf{D}_u)$  should be made as small as possible, that is, the minimum value of  $B(\mathbf{D}_u)$  is required. At this time, the partial derivatives of each component of  $B(\mathbf{D}_u)$  to the independent variables are all equal to zero, they are

$$\frac{\partial B(\mathbf{D}_u)}{\partial u_{x0}} = 0, \quad \frac{\partial B(\mathbf{D}_u)}{\partial u_{y0}} = 0, \quad \frac{\partial B(\mathbf{D}_u)}{\partial u_{xx0}} = 0, \quad \frac{\partial B(\mathbf{D}_u)}{\partial u_{yy0}} = 0, \quad \frac{\partial B(\mathbf{D}_u)}{\partial u_{xy0}} = 0 \quad (9)$$

The above equations are sorted into linear equations as follows:

$$\mathbf{A} \mathbf{D}_u = \mathbf{b} \quad (10)$$

where  $\mathbf{A} = \mathbf{L}^T \boldsymbol{\omega} \mathbf{L}$ ,  $\mathbf{b} = \mathbf{L}^T \boldsymbol{\omega} \mathbf{U}$ ,  $\mathbf{L} = (\mathbf{L}_1^T, \mathbf{L}_2^T, \dots, \mathbf{L}_n^T)^T$ ,  $\mathbf{L}_i = \left( \Delta x_i, \Delta y_i, \frac{\Delta x_i^2}{2}, \frac{\Delta y_i^2}{2}, \Delta x_i \Delta y_i \right)$ ,  $\boldsymbol{\omega} = \text{diag}(\omega_1^2, \omega_2^2, \dots, \omega_n^2)$ ,

$$\mathbf{U} = (u_1 - u_0, u_2 - u_0, \dots, u_n - u_0)^T.$$

Then, the above equation is rewritten as

$$\mathbf{D}_u = (u_{x0}, u_{y0}, u_{xx0}, u_{yy0}, u_{xy0})^T = \mathbf{A}^{-1} \mathbf{b} = \mathbf{A}^{-1} \mathbf{L}^T \boldsymbol{\omega} \mathbf{U} = \mathbf{M} \mathbf{U} \quad (11)$$

where  $\mathbf{M} = \mathbf{A}^{-1} \mathbf{L}^T \boldsymbol{\omega}$ .

For the convenience of notation, the elements of the matrix  $\mathbf{M}$  are denoted as  $m_{ij}$ , and it is not difficult to obtain the estimation of the partial derivatives at the central node  $M_0$  from the matrix as follows:

$$\begin{aligned} \frac{\partial u}{\partial x} &= \sum_{j=1}^n m_{1j} (u_j - u_0), \quad \frac{\partial u}{\partial y} = \sum_{j=1}^{n+1} m_{2j} (u_j - u_0), \quad \frac{\partial^2 u}{\partial x^2} = \sum_{j=1}^{n+1} m_{3j} (u_j - u_0), \quad \frac{\partial^2 u}{\partial y^2} = \sum_{j=1}^{n+1} m_{4j} (u_j - u_0), \\ \frac{\partial^2 u}{\partial x \partial y} &= \sum_{j=1}^{n+1} m_{5j} (u_j - u_0) \end{aligned} \quad (12)$$

As can be seen from Eq. (12), GFDM is very flexible to obtain the estimation expressions of the first-order derivative and the second-order derivative at the central node only according to the coordinates of the node included in the influence domain of the central node, therefore, the discretization of partial differential equations can be realized only under the condition of node allocation of the computational domain, without grid division. This is the most significant advantage of meshless GFDM compared with finite element and finite volume method based on mesh division.

### 2.3 GFDM based discrete schemes

For node  $i$ , suppose node  $j$  to be in the influence domain of node  $i$ , and the influence domain of node  $i$  totally contains  $n_i$  nodes except node  $i$ . According to Eq. (12), based on GFDM, it is obtained that:

$$\frac{\partial^2 p}{\partial x^2} = \sum_{j=1}^{n_i} m_{3,j}^i (p_{(i,j)} - p_i), \quad \frac{\partial^2 p}{\partial y^2} = \sum_{j=1}^{n_i} m_{4,j}^i (p_{(i,j)} - p_i) \quad (13)$$

where the superscript  $i$  of  $m_{3,j}^i$  indicates that node  $i$  is the central node and  $(i, j)$  denotes the serial number of the  $j$ -th node in the influence domain of node  $i$  in all nodes in the computing domain.

Then, the Laplace operator of pressure is approximated as follows:

$$\nabla \cdot (\nabla p) = \frac{\partial^2 p}{\partial x^2} + \frac{\partial^2 p}{\partial y^2} \approx \sum_{j=1}^{n_i} [(m_{3,j}^i + m_{4,j}^i) (p_{(i,j)} - p_i)] \quad (14)$$

For the actual underground reservoir, permeability  $k$  is often difficult to express as an explicit function about coordinates, but only knows the permeability value at some node, therefore, it is difficult for us to take  $k$  as a function and extract it from the diffusion term. Therefore, this paper uses the harmonic average scheme of the permeability nodal value to calculate the permeability between node  $i$  and node  $j$ , the arithmetic average scheme of the viscosity nodal value is used to characterize the fluid viscosity between node  $i$  and node  $j$ , this method of dealing with the heterogeneity of physical parameters is beneficial to the easier application of GFDM in practical physical problems, because it is generally difficult to obtain the function expression of physical parameters with good smoothness in practical physical problems, especially the related physical parameters of underground reservoirs. The numerical examples in section 3.3 will prove that such treatment can achieve sufficient calculation accuracy. Therefore, it is obtained that:

$$\nabla \cdot \left( \frac{k}{\mu(T)} \nabla p \right) = \sum_{j=1}^{n_i} \frac{k_{ij}}{\mu_{ij}} [(m_{3,j}^i + m_{4,j}^i) (p_{(i,j)} - p_i)] \quad (15)$$

$$\text{Where } k_{ij} = \frac{2k_i k_{(i,j)}}{k_i + k_{(i,j)}}, \quad \mu_{ij} = \frac{\mu(T_i) + \mu(T_{(i,j)})}{2}.$$

For the heat convection-diffusion equation, the heat conduction term in Eq. (2) can adopt a discrete scheme similar to Eq. (14), and obtain:

$$\nabla(\lambda_c(p, T) \nabla T) = \sum_{j=1}^{n_i} \lambda_{c,ij} \left[ (m_{3,j}^i + m_{4,j}^i) (T_{(i,j)} - T_i) \right] \quad (16)$$

where  $\lambda_{c,ij} = \frac{2\lambda_{c,i}\lambda_{c,(i,j)}}{\lambda_{c,i} + \lambda_{c,(i,j)}}$ ,  $\lambda_{c,i} = \lambda_c(p_i, T_i)$ ,  $\lambda_{c,(i,j)} = \lambda_c(p_{(i,j)}, T_{(i,j)})$ .

For the heat convection term in Eq. (2), it can be seen that since the fluid velocity term in the convection term is related to the pressure gradient, the convection term has a form similar to the pressure diffusion term, therefore, the approximation scheme of the diffusion term in GFDM can be effectively used to approximate the heat convection term, thus obtaining Eq. (17). However, it should be noted that the convection term has asymmetry, so the parameter  $T_{ij}$  in Eq. (17) needs to take the upwind scheme. In a meshless method, the upstream effect is generally constructed by modifying the influence domain, however, this method is not conducive to the construction of a general framework and may affect the calculation accuracy of pressure diffusion equations or other equations in the multi-physics coupling problem, therefore, this paper constructs the upstream scheme without modifying the influence domain. We think that, although GFDM is a meshless method, it also has the characteristics of FDM. Therefore, GFDM may be able to directly learn from the upwind scheme in FDM. Inspired by this idea, the upwind scheme of temperature in Eq. (18) is adopted, which will be verified to obtain a high-accuracy solution in Section 3.

$$\nabla \left( \rho C_p T \frac{k}{\mu} \nabla p \right) = \sum_{j=1}^{n_i} \left[ \rho C_p T_{ij} \frac{k_{ij}}{\mu_{ij}} (m_{3,j}^i + m_{4,j}^i) (p_{(i,j)} - p_i) \right] \quad (17)$$

$$T_{ij} = \begin{cases} T_{(i,j)} & \text{if } p_{(i,j)} \geq p_i \\ T_i & \text{if } p_{(i,j)} < p_i \end{cases} \quad (18)$$

In order to reduce the difficulty of programming calculation, a full implicit coupled schemes is not adopted to simultaneously solve the nodal pressure and temperature, but a sequential coupled scheme is adopted, that is, based on the temperature values of n time steps, implicitly calculate the pressure values of n+1 time step, and then calculate the temperature values of n+1 time step.

Therefore, the discrete scheme of the right side of the pressure diffusion equation is as follows:

$$\frac{\partial \phi(p, T)}{\partial t} = \frac{\partial \phi(p, T^n)}{\partial t} = \left[ 1 + \frac{(1-\phi_0)}{\phi_0} C_{Temp} (T^n - T_0) \right] C_i \frac{\partial p}{\partial t} = \left[ 1 + \frac{(1-\phi_0)}{\phi_0} C_{Temp} (T^n - T_0) \right] C_i \frac{p^{n+1} - p^n}{\Delta t} \quad (19)$$

Then the discrete scheme of Eq. (1) is obtained as follows:

$$0.0864 \sum_{j=1}^{n_i} \frac{k_{ij}}{\mu_{ij}} \left[ (m_{3,j}^i + m_{4,j}^i) (p_{(i,j)}^{n+1} - p_i^{n+1}) \right] + q_i^{n+1} = \left[ 1 + \frac{(1-\phi_0)}{\phi_0} C_{Temp} (T_i^n - T_0) \right] C_i \frac{p_i^{n+1} - p_i^n}{\Delta t} \quad (20)$$

When the source or sink term is zero, the linear equation is sorted as follows:

$$0.0864 \sum_{j=1}^{n_i} \frac{k_{ij}}{\mu_{ij}^n} (m_{3,j}^i + m_{4,j}^i) p_{(i,j)}^{n+1} - \left( 0.0864 \sum_{j=1}^{n_i} \frac{k_{ij}}{\mu_{ij}^n} (m_{3,j}^i + m_{4,j}^i) + \frac{1}{\Delta t} \left[ 1 + \frac{(1-\phi_0)}{\phi_0} C_{Temp} (T_i^n - T_0) \right] \right) C_i p_i^{n+1} + q_i^{n+1} = -\frac{1}{\Delta t} \left[ 1 + \frac{(1-\phi_0)}{\phi_0} C_{Temp} (T_i^n - T_0) \right] C_i p_i^n \quad (21)$$

where  $\mu_{ij}^n = \frac{\mu(T_i^n) + \mu(T_j^n)}{2}$ .

By synthesizing the discrete pressure diffusion equation at each node, combined with the boundary condition (the detailed treatment of boundary condition is illustrated in Section 2.4, global linear equations can be obtained to solve nodal pressure at n+1 time step. Then, the discrete equations of Eq. (2) about temperature distribution are obtained:

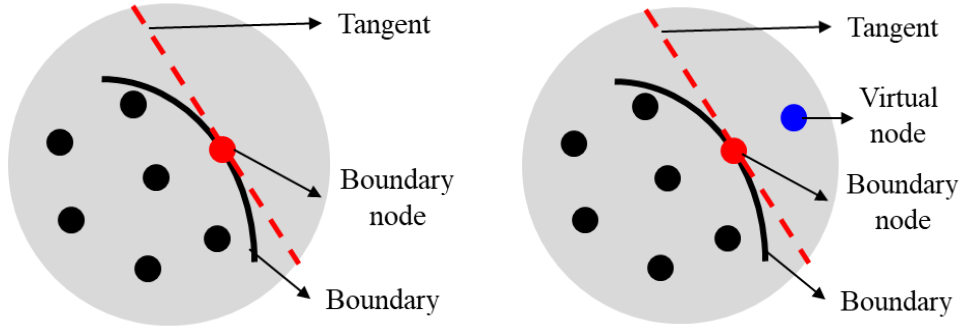
$$86400 \sum_{j=1}^{n_i} \left[ \lambda_{c,ij} (p^{n+1}, T^n) (m_{3,j}^i + m_{4,j}^i) (T_{(i,j)}^{n+1} - T_i^{n+1}) \right] + 0.0864 \sum_{j=1}^{n_i} \left[ \rho_l C_l T_{ij}^{n+1} \frac{k_{ij}}{\mu_{ij}^n} (m_{3,j}^i + m_{4,j}^i) (p_{(i,j)}^{n+1} - p_i^{n+1}) \right] \quad (22)$$

$$+ q_H^{n+1} = \frac{\left[ ((1 - \phi_i^{n+1}) \rho_R C_R + \phi_i^{n+1} \rho_l C_l) T_i^{n+1} \right] - \left[ ((1 - \phi_i^n) \rho_R C_R + \phi_i^n \rho_l C_l) T_i^n \right]}{\Delta t}$$

where  $\phi_i^{n+1} = \phi(p_i^{n+1}, T^n)$ ,  $\phi_i^n = \phi(p_i^n, T^n)$ ,  $\mu_{ij}^n = \frac{\mu(T_i^n) + \mu(T_{(i,j)}^n)}{2}$ ,  $T_{ij} = \begin{cases} T_{(i,j)} & \text{if } p_{(i,j)} \geq p_i \\ T_i & \text{if } p_{(i,j)} < p_i \end{cases}$ .

## 2.4 Treatment of boundary conditions

Since the meshless method including GFDM determines the distribution information of unknown quantities in the local influence domain of the central node only based on the geometric information of all nodes in the influence domain, for example, GFDM used in this paper uses the information of relative coordinates of all nodes in the influence domain to the central node to construct the approximation scheme of the first-order partial derivative and second-order partial derivative of the unknown function at the central node. Therefore, the relative coordinates of all nodes in the influence domain to the central node is crucial to the accuracy of estimation of physical quantities in the local influence domain. As shown in Fig. 1, for nodes (red solid points) on the boundary, the nodes (black solid points) in the influence domain (gray area) of the boundary node are all on one side of the tangent line (red dotted line) at this boundary node, so the estimation accuracy of derivatives at this boundary node by using these nodes is low, resulting in low overall calculation accuracy. Therefore, the calculation accuracy of the meshless method is sensitive to derivative boundary conditions (such as Neuman boundary condition and Rudin boundary condition). Therefore, as shown in Fig. 1, in this paper, derivative boundary conditions are improved by adding virtual nodes (blue solid points) on the other side of the tangent to improve the estimation accuracy of the derivatives. Next, this section takes pressure calculation as an example to illustrate the specific processing details of the derivative boundary conditions.



(a) the original case (b) the case after adding the virtual node

Fig. 1 Sketch of adding virtual nodes

Assume that there are  $n_1$  internal nodes in the computing domain,  $n_2$  nodes meeting Dirichlet boundary conditions, and  $n_3$  nodes meeting derivative boundary conditions. For the convenience of depiction, assume here that the expressions of the Dirichlet boundary condition and the derivative boundary condition are:

$$p|_A = p_1, \quad \left( \alpha p + \beta \frac{\partial p}{\partial x} \right) \Big|_B = \gamma \quad (23)$$

where  $A$  and  $B$  are the nodes that meet the boundary conditions of the first type and the derivative type respectively,  $\alpha$ ,  $\beta$  and  $\gamma$  are coefficients.

For node  $A$  that meets the Dirichlet boundary condition, if the sequence number of the node  $A$  in all nodes is  $a$ , the equation corresponding to the boundary condition is:

$$p_a^{n+1} = p_1 \quad (24)$$

For node  $B$  that meets derivative boundary conditions, set the serial number of node  $B$  in all nodes is  $b$ , and add the virtual node corresponding to node  $B$ , denoted as node  $C$ , because each derivative-boundary-condition node needs to add a corresponding virtual node, the number of nodes in the entire computing domain is  $n_1+n_2+n_3+n_3$ , if the serial number of the virtual node  $C$  in all nodes is  $c$ , the equation at node  $B$  is no longer the equation corresponding to the boundary condition, but the Eq. (25) which is the same as the Eq. (19) of an inner node, and the equation corresponding to the boundary condition is used as the equation corresponding to virtual node  $C$ . They are:

Node  $B$ :

$$0.0864 \sum_{j=1}^{n_b} \frac{k_{bj}}{\mu_{bj}} \left[ (m_{3,j}^b + m_{4,j}^b) (p_{(b,j)}^{n+1} - p_b^{n+1}) \right] + q_b^{n+1} = \left[ 1 - \frac{(1-\phi_0)}{\phi_0} C_{Temp} (T_b^n - T_0) \right] C_t \frac{p_b^{n+1} - p_b^n}{\Delta t} \quad (25)$$

Node  $C$ :

$$\left( \alpha p + \beta \frac{\partial p}{\partial x} \right) \Big|_B = \alpha p_b + \beta \sum_j^{n_b} m_{1j} p_{(b,j)} = \gamma \quad (26)$$

where  $n_b$  is the number of nodes in the influence domain of node  $B$ ,  $(b, j)$  is the serial number of the  $j$ -th node in the influence domain of node  $B$  in all nodes of the entire computing domain. As you can know, there is a  $j$  that meets  $(b, j) = c$ .

Finally, the linear equations composed of  $n_1+n_2+n_3+n_4$  equations can be obtained in the entire computational domain, including  $n_1$  Eq. (19),  $n_2$  Eq. (24),  $n_3$  Eq. (25) and  $n_4$  Eq. (26), thus solving the linear equations in a closed manner to obtain the pressure values of all nodes (including  $n_1$  interior nodes,  $n_2+n_3$  boundary nodes and  $n_3$  virtual nodes) at  $n+1$  time step. Combined with Eq. (22) and boundary conditions about temperature (using the same treatment of boundary conditions in this section) calculate the temperature values of all nodes at the  $n+1$  time step. Then continue to solve the pressure and temperature distribution at  $n+2$  time step.

### 3. Numerical examples

In this section, a numerical example is designed to verify the effectiveness of the upwind scheme in Eq. (18), and then two numerical examples are designed, including homogeneous and heterogeneous reservoir examples in the same irregular polygonal calculation domain, to validate the presented modeling of the single-phase heat and mass transfer.

#### 3.1 Validation of the upwind scheme

In this example, a regular rectangular computing domain ( $[0\text{m}, 300\text{m}] \times [0\text{m}, 100\text{m}]$ ) is selected. The values of relevant physical parameters are shown in Table 1. In this paper, the upstream scheme only involves the thermal convection term, so in this example, compressibility coefficient, thermal expansion coefficient and viscosity-temperature coefficient are 0, and the upper and lower boundaries are closed boundary conditions, the left and right boundaries are constant pressure and fixed temperature boundary conditions. For specific equations, see Eq. (27) and Eq. (28), thus constructing a stable flow field independent of temperature distribution, in order to better control other variables and only analyze the effectiveness of the upwind scheme in Eq. (18).

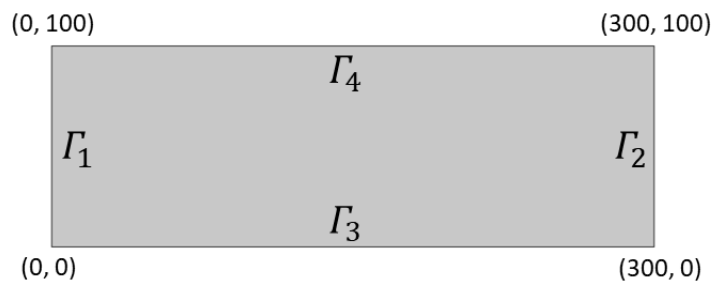


Fig. 2 Sketch of the rectangular calculation domain

Table 1 Values of physical properties of the numerical case

Permeability $k$	500 mD
Heat conduction coefficient of fluid $\lambda_l$	0.2 J/s/m/°C
Heat conduction coefficient of rock $\lambda_r$	3 J/s/m/°C
Heat capacity of fluid $C_l$	$4.2 \times 10^3$ J/KG/°C
Heat capacity of rock $C_R$	200 J/KG/°C
Fluid density $\rho_l$	1000 kg/m <sup>3</sup>
Rock density $\rho_R$	2700 kg/m <sup>3</sup>
Initial porosity $\phi_0$	0.3
Compressibility coefficient $C_i$	0 MPa <sup>-1</sup>
Thermal expansion coefficient $C_{Temp}$	0 MPa <sup>-1</sup>
Fluid viscosity at initial temperature $\mu(T_0)$	5 mPa·s
Viscosity-temperature coefficient $\alpha_T$	0 °C <sup>-1</sup>

$$\nabla \cdot (\nabla p) = 0, \quad p|_{\Gamma_1} = 15, \quad p|_{\Gamma_2} = 10, \quad \frac{\partial p}{\partial y}|_{\Gamma_3} = 0, \quad \frac{\partial p}{\partial y}|_{\Gamma_4} = 0 \quad (27)$$

$$186624 \nabla^2 T + 36288000 \nabla \cdot (T \nabla p) = 1638000 \frac{\partial T}{\partial t}, \quad T|_{\Gamma_1} = 15, \quad T|_{\Gamma_2} = 10, \quad \frac{\partial T}{\partial y}|_{\Gamma_3} = 0, \quad \frac{\partial T}{\partial y}|_{\Gamma_4} = 0 \quad (28)$$

The analytical solution of Eq. (27) about pressure is:  $p = 15 - x/60$ .

So the pressure gradient (i.e., the flow velocity) is calculated as

$$\nabla p = \left( \frac{\partial p}{\partial x}, \frac{\partial p}{\partial y} \right) = \left( -\frac{1}{60}, 0 \right) \quad (29)$$

Then the Eq. (28) about temperature profile is the following convection-diffusion equation.

$$186624 \frac{\partial^2 T}{\partial x^2} - 604800 \frac{\partial T}{\partial x} = 1638000 \frac{\partial T}{\partial t}, \quad T|_{x=0} = 40, \quad T|_{x=300} = 60 \quad (30)$$

Since Eq. (30) is essentially a one-dimensional (1D) heat convection-diffusion problem, this section uses the calculation results of the one-dimensional upwind finite difference method (FDM) that meet the stability conditions as reference solutions to test the calculation performances of the upstream schemes in Eq. (18).

First, allocate nodes by supposing  $\Delta x = 10m$ ,  $\Delta y = 10m$ , then there are  $31 \times 11 = 341$  nodes in the calculation domain, and the radius of the node influence domain is  $r_e = 1.5\sqrt{\Delta x^2 + \Delta y^2}$ . Take the time step  $\Delta t = 1d$ , the comparison of the calculation results is shown in Fig. 3(a). It can be seen that the calculation results of the upwind scheme are very consistent with those of the 1D upwind FDM.

GFDM is a meshless method, in which, changing the radius of the influence domain can flexibly establish the adjacent relationship between nodes. Therefore, Fig. 3 (b), Fig. 3 (c) compare the calculation results under different radii of the influence domain ( $r_e = 1.001\sqrt{\Delta x^2 + \Delta y^2}$ ,  $r_e = 2.5\sqrt{\Delta x^2 + \Delta y^2}$ ,  $r_e = 3.5\sqrt{\Delta x^2 + \Delta y^2}$ , respectively) to test the calculation performance of the upwind scheme, and Table 2 lists the average relative errors at different radius of influence domain; It can be seen that the calculation results at different radius of the influence domain are all close to those of the upwind FDM, but the larger the radius of the influence domain, the calculation accuracy of upwind GFDM will decrease slightly.

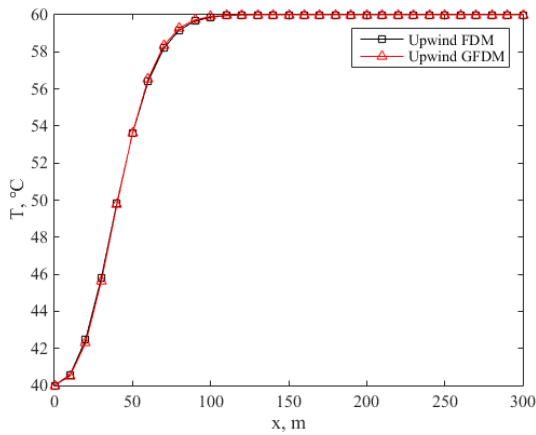
Then, in order to test the calculation effect of the upwind scheme under different space and time-step sizes, allocate nodes by supposing  $\Delta x = 5m$ ,  $\Delta y = 5m$ , and take the time step  $\Delta t = 0.5d$ . Fig. 3(d) compares the calculation results, and it can be seen that the calculation result of the upwind scheme is still very consistent with that of the upwind FDM.

Finally, to test the calculation effect of the upwind scheme under different-intensity convection terms,  $p|_{x=0} = 15$  is enhanced to  $p|_{x=0} = 25$ , then Eq. (30) is changed to Eq. (31). At this time, as shown in Fig. 3(e), the upwind scheme can still achieve almost identical results.

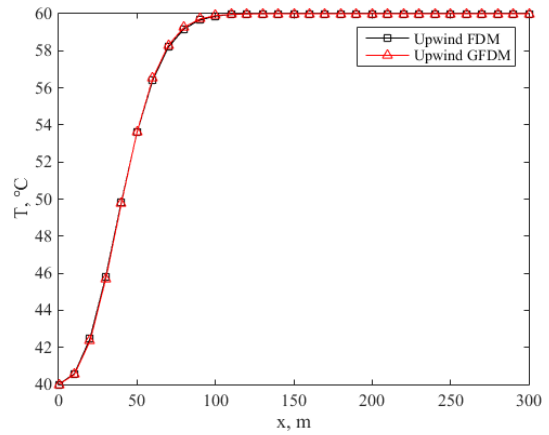
$$186624 \frac{\partial^2 T}{\partial x^2} - 1814400 \frac{\partial T}{\partial x} = 1638000 \frac{\partial T}{\partial t}, \quad T|_{x=0} = 40, \quad T|_{x=300} = 60 \quad (31)$$

The comparison results in Fig. 3 fully demonstrate the accuracy of the upwind scheme in GFDM. In addition, the cases in Sections 3.2 and 3.3 will show that the upwind GFDM can still achieve good results

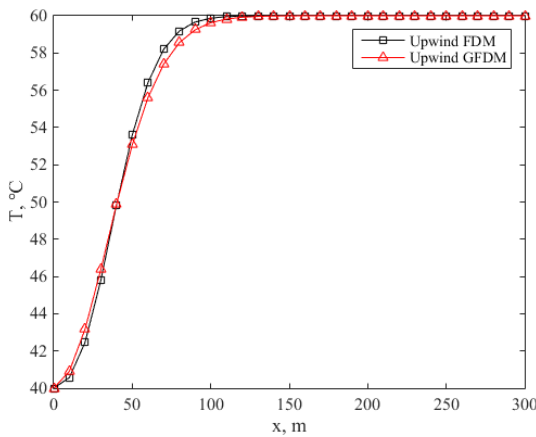
under the condition of irregular collocation nodes, and Section 3.4 will point out that the upwind GFDM for the single-phase heat and mass transfer problem can be used to realize a high-accuracy solution of convection-diffusion equation.



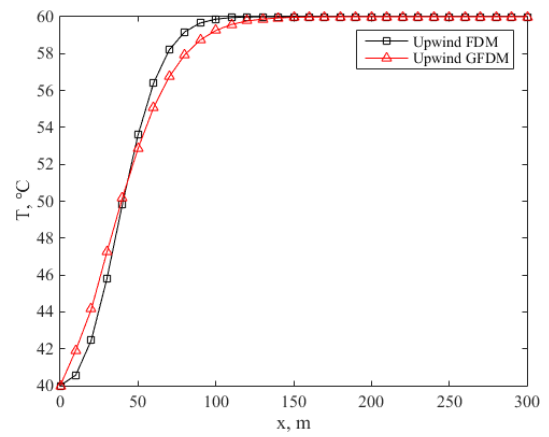
(a)  $\Delta x = 10m, \Delta y = 10m, \Delta t = 1d, p|_{x=0} = 15,$   
 $r_e = 1.5\sqrt{\Delta x + \Delta y}$



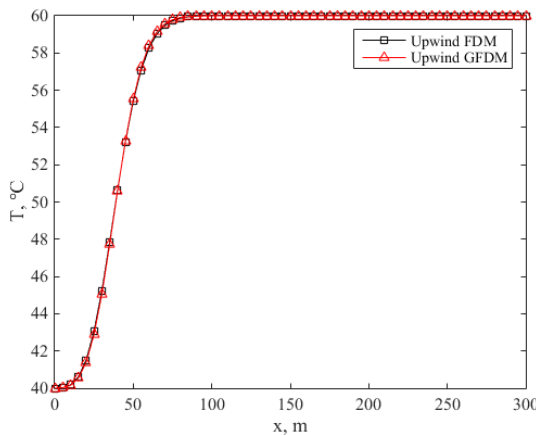
(b)  $\Delta x = 10m, \Delta y = 10m, \Delta t = 1d, p|_{x=0} = 15,$   
 $r_e = 1.001\sqrt{\Delta x + \Delta y}$



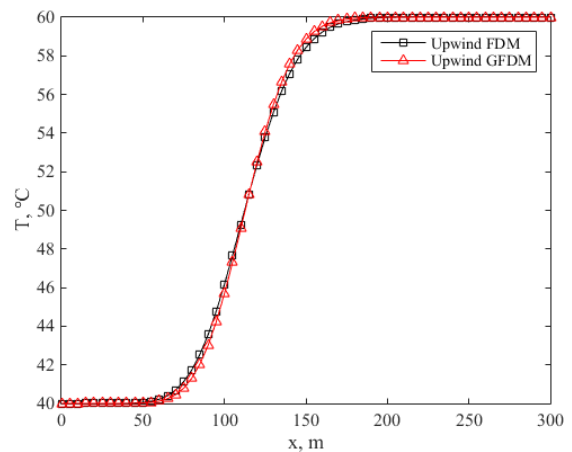
(c)  $\Delta x = 10m, \Delta y = 10m, \Delta t = 0.5d, p|_{x=0} = 15,$   
 $r_e = 2.5\sqrt{\Delta x + \Delta y}$



(d)  $\Delta x = 10m, \Delta y = 10m, \Delta t = 1d, p|_{x=0} = 15,$   
 $r_e = 3.5\sqrt{\Delta x + \Delta y}$



(e)  $\Delta x = 5m, \Delta y = 5m, \Delta t = 0.5d, p|_{x=0} = 15,$   
 $r_e = 1.5\sqrt{\Delta x + \Delta y}$



(f)  $\Delta x = 5m, \Delta y = 5m, \Delta t = 0.5d, p|_{x=0} = 25,$   
 $r_e = 1.5\sqrt{\Delta x + \Delta y}$

图 3 迎风 GFDM 及迎风 FDM 的计算结果对比

Table 2 Average relative errors at different radius of influence domain

Radius of influence domain	$r_e = 1.001\sqrt{\Delta x^2 + \Delta y^2}$	$r_e = 1.5\sqrt{\Delta x^2 + \Delta y^2}$	$r_e = 2.5\sqrt{\Delta x^2 + \Delta y^2}$	$r_e = 3.5\sqrt{\Delta x^2 + \Delta y^2}$
Average relative error	0.0528%	0.0705%	0.3286%	0.7547%

### 3.2 A case with homogeneous formation

As shown in Fig. 4, this example is an irregular polygonal computing domain. Eq. (32) and Eq. (33) show the boundary conditions and initial value conditions about pressure and temperature respectively. The left boundary and the right boundary are Dirichlet boundary conditions, and the upper and lower boundaries are closed boundary conditions. The values of relevant physical parameters are shown in Table 3. It can be seen that the permeability in the calculation domain of this example is a constant, representing a homogeneous porous reservoir.

$$p|_{\Gamma_1} = 15\text{MPa}, \quad p|_{\Gamma_2} = 10\text{MPa}, \quad p_0 = 10\text{MPa}, \quad \frac{\partial p}{\partial y}|_{\Gamma_3} = 0\text{MPa/m}, \quad \frac{\partial p}{\partial y}|_{\Gamma_4} = 0\text{MPa/m} \quad (32)$$

$$T|_{\Gamma_1} = 40^\circ\text{C}, \quad T|_{\Gamma_2} = 60^\circ\text{C}, \quad T_0 = 60^\circ\text{C}, \quad \frac{\partial T}{\partial y}|_{\Gamma_3} = 0^\circ\text{C/m}, \quad \frac{\partial T}{\partial y}|_{\Gamma_4} = 0^\circ\text{C/m} \quad (33)$$

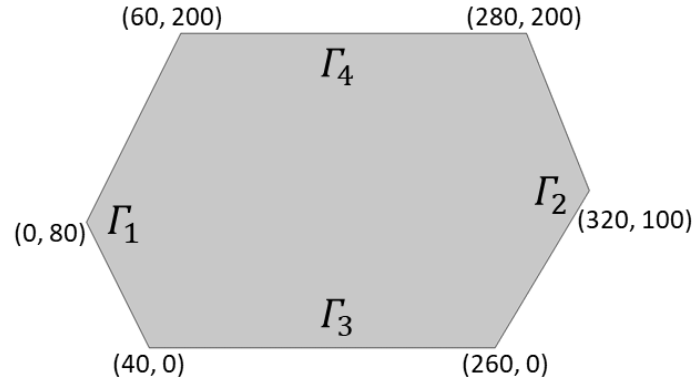


Fig. 4 The computational domain of example 2

Table 3 Values of physical properties of the numerical case

Permeability (k)	500 mD
Heat conduction coefficient of fluid $\lambda_f$	0.2 J/s/m/°C
Heat conduction coefficient of rock $\lambda_r$	3 J/s/m/°C
Heat capacity of fluid $C_f$	$4.2 \times 10^3$ J/KG/°C
Heat capacity of rock $C_R$	200 J/KG/°C
Fluid density $\rho_f$	1000 kg/m <sup>3</sup>
Rock density $\rho_R$	2700 kg/m <sup>3</sup>
Initial porosity $\phi_0$	0.3
Coefficient of compressibility $C_i$	$1 \times 10^{-5}$ MPa <sup>-1</sup>
Coefficient of thermal expansion $C_{Temp}$	$1 \times 10^{-5}$ MPa <sup>-1</sup>
Fluid viscosity at initial temperature $\mu(T_0)$	5 mPa·s
Viscosity-temperature coefficient $\alpha_T$	0.05 °C <sup>-1</sup>

Fig. 5 shows the fine triangular mesh for FEM, rough triangular mesh for FEM and the collocation nodes used for GFDM calculation in this example, and the collocation nodes come from the nodes in the rough triangular mesh. It should be pointed out that in this example, for the convenience of comparison, the nodes in the rough triangular mesh are selected as the collocation nodes of the calculation domain. In fact, we can flexibly select other collocation nodes. Compared with the mesh generation of the computational domain, the node collocation in the computational domain is much more flexible and easy, which is also one of the important advantages of the presented upwind GFDM compared with the mesh-based method. In this example, the finite element solution based on the fine triangular mesh shown in Fig. 5(a) is used as the reference solution, and the finite element solution based on the rough triangular mesh in Fig. 5(b) and the upwind GFDM solution based on allocation nodes in Fig. 5(c) are calculated respectively. In addition, in the calculation process of the upwind GFDM in this paper, since boundaries 2 and 3 are the second type of boundary conditions, as described in Section 2.4, Fig. 6(a) adds a red node as a virtual point 20m perpendicular to the boundary direction at each blue boundary node to better describe the second type of boundary conditions, and the radius of node influence

domain is set to  $r_c = 30m$ , which can guarantee the added virtual node is included in the influence domain of corresponding derivative-boundary-condition node and there are at least 5 other nodes are included in influence domain of each node except virtual nodes, so it can be solved effectively by GFDM. The time step is set as  $\Delta t = 1d$ .

In this section, 8 nodes shown in Fig. 6(b) are selected to compare the calculation results of FEM and upwind GFDM in this paper. Fig. 7 shows the reference solution of temperature and pressure distribution based on fine triangulation from COMSOL software. It can be seen that the first to fourth nodes are selected in the area where the temperature distribution changes significantly due to the influence of heat convection, The 5th to 8th nodes are selected in the area almost unaffected by heat convection. Table 4 lists the calculated temperature and pressure data of each node in detail. It can be seen that the average computational error of GFDM on node temperature at  $P_1, P_2, P_3,$  and  $P_4$  is 1.6670%, while the average error of FEM is 4.7739%, which shows that the GFDM in this paper has higher calculation accuracy than FEM in the area with significant influence of thermal convection, and also shows the effectiveness of scheme 3 in Section 3.1. Moreover, GFDM has achieved comparable accuracy as FEM for nodal values from  $P_5$  to  $P_8$ . Considering the advantages of upwind GFDM, which does not rely on mesh generation and only needs to allocate nodes in the computational domain, the comparison results of this example show that upwind GFDM has certain advantages over FEM in computational accuracy and computational difficulty.

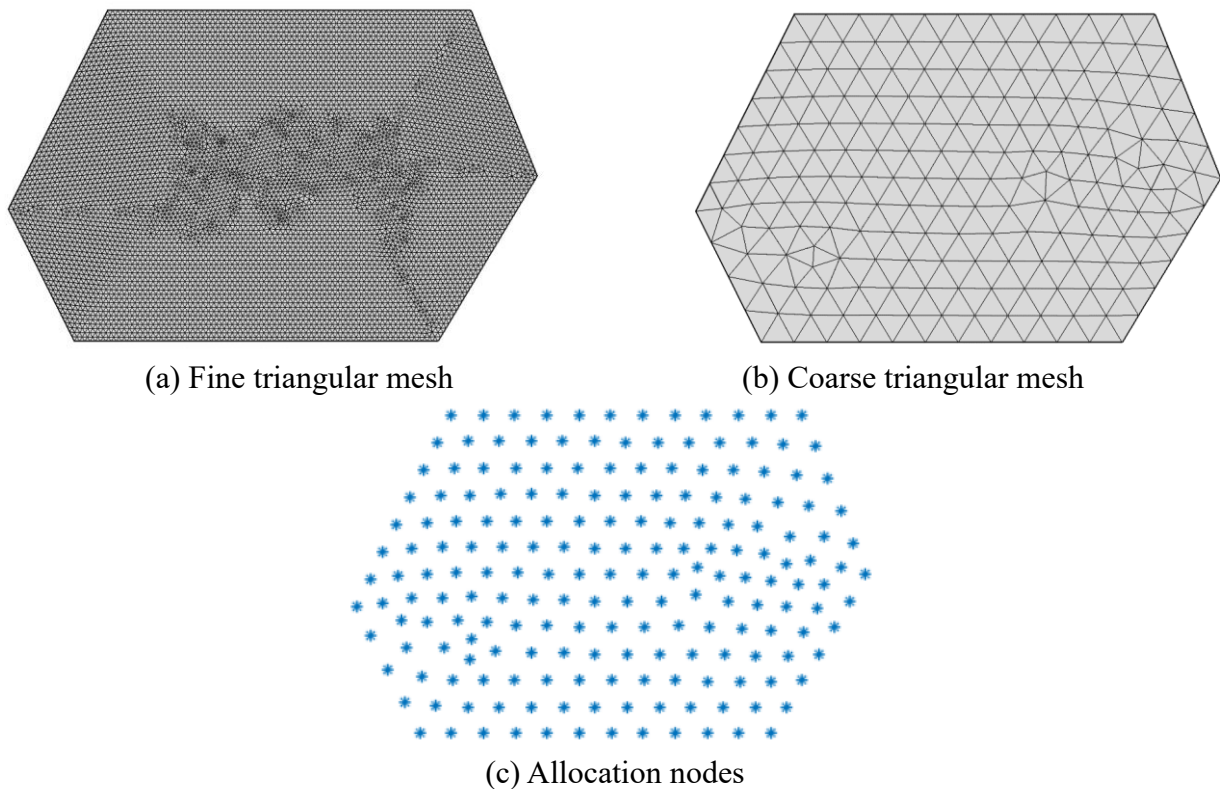


Figure 5 Geometric characterization of computational domain

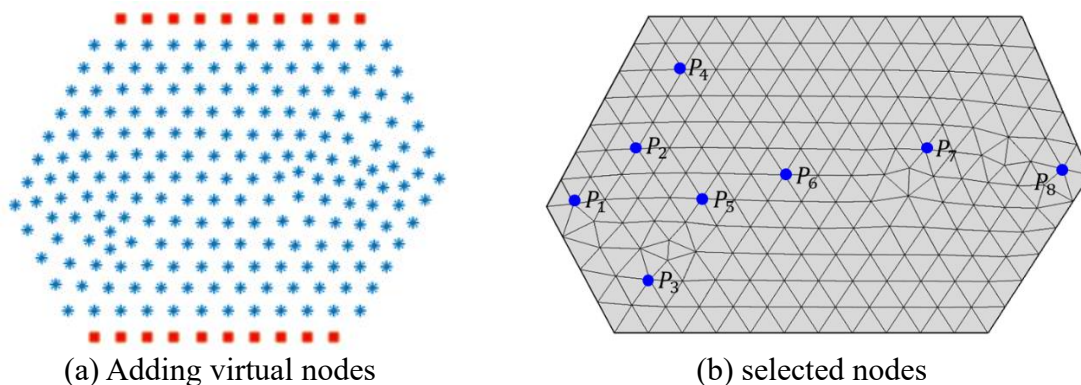


Fig. 6 location diagram of virtual nodes in computing domain and nodes used for result comparison

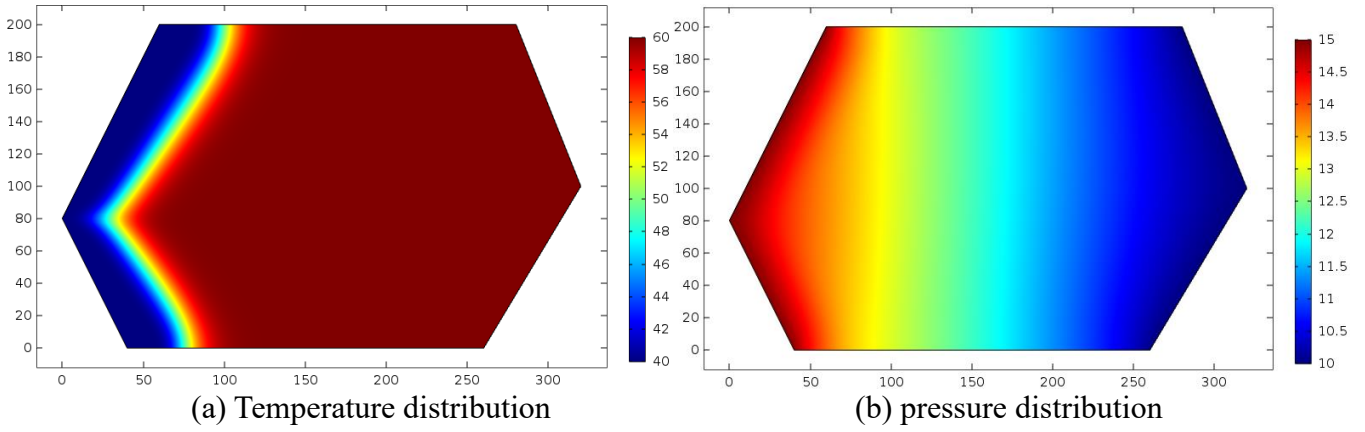


Fig. 7 Reference solution by FEM based on fine triangular mesh

Table 4 Comparison of results at selected nodes in example 2

Nodes	$P_1 (16.25, 81.7265)$		$P_2 (52.882, 116.04)$		$P_3 (60.144, 34.942)$		$P_4 (80.720, 166.27)$	
	$T(^{\circ}\text{C})$	$p(\text{MPa})$	$T(^{\circ}\text{C})$	$T(^{\circ}\text{C})$	$T(^{\circ}\text{C})$	$p(\text{MPa})$	$T(^{\circ}\text{C})$	$p(\text{MPa})$
GFDM	43.2405	14.7273	47.8228	13.9969	47.3392	13.8054	51.8557	13.0977
FEM	41.2600	14.7189	45.8944	13.9239	45.1921	13.7233	52.9444	13.0265
Exact	42.6606	14.6366	48.5429	13.9241	48.6942	13.7074	51.3206	13.2547
Error of GFDM	1.3594%	0.6201%	1.4835%	0.5234%	2.7827%	0.7148%	1.0426%	1.1843%
Error of FEM	3.2832%	0.5628%	5.4562%	0.0011%	7.1920%	0.1162%	3.1641%	1.7214%
Nodes	$P_5 (90.404, 84.568)$		$P_6 (140.03, 100.30)$		$P_7 (222.33, 116.04)$		$P_8 (304.64, 102.12)$	
	$T(^{\circ}\text{C})$	$p(\text{MPa})$	$T(^{\circ}\text{C})$	$p(\text{MPa})$	$T(^{\circ}\text{C})$	$p(\text{MPa})$	$T(^{\circ}\text{C})$	$p(\text{MPa})$
GFDM	56.4969	13.4891	59.8931	12.3329	60.0023	11.0628	60.0005	10.0872
FEM	59.2950	13.4301	59.9892	12.3296	60.0000	11.0660	60.0000	10.0858
Exact	59.9700	13.3541	60.0000	12.3804	60.0000	11.0983	60.0000	10.0830
Error of GFDM	5.7915%	1.0104%	0.1782%	0.3837%	0.0039%	0.3199%	0.0009%	0.0413%
Error of FEM	1.1256%	0.5686%	0.0180%	0.4102%	0.0000%	0.2911%	0.0000%	0.0273%

### 3.3 A case with heterogeneous formation

In order to verify the effectiveness of the treatment of heterogeneous reservoir physical parameters in this paper, this example constructs a heterogeneous reservoir permeability distribution characterized by Eq. (34). The calculation domain, boundary conditions, the mesh division, and allocation nodes are the same as those in example 2, and the values of other physical parameters except permeability are also the same.

$$k = 800e^{-x/320} \quad (34)$$

Table 4 compares the calculation results of upwind GFDM and FEM in this paper, where the average computational error of upwind GFDM on node temperature at  $P_1, P_2, P_3$  and  $P_4$  is 1.6433%, while the average error of FEM is 4.5477%. The calculation accuracy of upwind GFDM for temperature in the region where temperature changes significantly is still generally higher than that FEM, moreover, the treatment of permeability does not use the above-mentioned functional expression, but only uses the permeability value of each node calculated by the function, and still can obtain the accuracy of pressure and temperature comparable to FEM, this shows that the treatment of the heterogeneity of physical parameters in Eq. (15) is reasonable, thus providing a simple and effective idea for the application of upwind GFDM to heterogeneous complex physical problems, and enhance the application potential of upwind GFDM in practical physical problems.

Table 5 Comparison of results at selected nodes in example 3

Nodes	$P_1 (16.25, 81.7265)$		$P_2 (52.882, 116.04)$		$P_3 (60.144, 34.942)$		$P_4 (90.404, 84.568)$	
	$T(^{\circ}\text{C})$	$p(\text{MPa})$	$T(^{\circ}\text{C})$	$p(\text{MPa})$	$T(^{\circ}\text{C})$	$p(\text{MPa})$	$T(^{\circ}\text{C})$	$p(\text{MPa})$
GFDM	43.1018	14.8157	47.8858	14.2827	47.4592	14.1363	52.3434	13.5557
FEM	41.1975	14.8100	46.1225	14.2312	45.4772	14.0775	53.6435	13.5051
Exact	42.5094	14.7548	48.7796	14.2360	49.0491	14.0708	52.3989	13.6989
Error of GFDM	1.3937%	0.4125%	1.8324%	0.3282%	3.2414%	0.4652%	0.1059%	1.0453%
Error of FEM	3.0862%	0.3744%	5.4471%	0.0341%	7.2824%	0.0476%	2.3753%	1.4147%
Nodes	$P_4 (90.404, 84.568)$		$P_6 (140.03, 100.30)$		$P_7 (222.33, 116.04)$		$P_8 (304.64, 102.12)$	

	$T(^{\circ}\text{C})$	$p(\text{MPa})$	$T(^{\circ}\text{C})$	$p(\text{MPa})$	$T(^{\circ}\text{C})$	$p(\text{MPa})$	$T(^{\circ}\text{C})$	$p(\text{MPa})$
GFDM	56.4604	13.8941	59.9028	12.8786	60.0031	11.4833	60.0007	10.1377
FEM	59.1492	13.8542	59.9917	12.8839	60.0000	11.4918	60.0000	10.1359
Exact	59.9713	13.7997	60.0000	12.9363	60.0000	11.5304	60.0000	10.1312
Error of GFDM	5.8542%	0.6842%	0.1620%	0.4461%	0.0052%	0.4084%	0.0012%	0.0645%
Error of FEM	1.3709%	0.3947%	0.0138%	0.4048%	0.0000%	0.3350%	0.0000%	0.0461%

### 3.4. An upwind GFDM for solution of convection-diffusion equation with constant coefficients

Different from the diffusion equation, an asymmetric convection term is added to the convection-diffusion equation. When the convection effect is relatively strong, theoretically, it is often necessary to use the upstream weight treatment to discretize the convection term to eliminate the oscillation of the solution caused by the asymmetry of the convection term.

The numerical examples in Sections 3.1, 3.2, and 3.3 demonstrate that the upwind GFDM in this paper can realize the high-accuracy meshless calculation of single-phase heat and mass transfer. Therefore, this paper aims to obtain the high-precision solution of the convection-diffusion equation by solving a single-phase heat and mass transfer problem which is equivalent to the convection-diffusion problem.

Assuming that the flow velocity field  $\mathbf{V}=(v_x, v_y)$  has been calculated, if it is a steady physical field, the temperature distribution of the flow field is characterized by the following convection-diffusion equation:

$$\frac{\partial}{\partial x}\left(k_x \frac{\partial T}{\partial x}\right) + \frac{\partial}{\partial y}\left(k_y \frac{\partial T}{\partial y}\right) - v_x \frac{\partial T}{\partial x} - v_y \frac{\partial T}{\partial y} = 0 \quad (35)$$

where  $k_x$  and  $k_y$  are heat conduction coefficients in x and y directions, respectively.

If it is an unsteady physical field, the temperature distribution of the flow field meets:

$$\frac{\partial}{\partial x}\left(k_x \frac{\partial T}{\partial x}\right) + \frac{\partial}{\partial y}\left(k_y \frac{\partial T}{\partial y}\right) - v_x \frac{\partial T}{\partial x} - v_y \frac{\partial T}{\partial y} = C \frac{\partial T}{\partial t} \quad (36)$$

Suppose the general form of the convection-diffusion equation as follows:

$$\frac{\partial}{\partial x}\left(k_x \frac{\partial T}{\partial x}\right) + \frac{\partial}{\partial y}\left(k_y \frac{\partial T}{\partial y}\right) - v_x \frac{\partial T}{\partial x} - v_y \frac{\partial T}{\partial y} = C \frac{\partial T}{\partial t} \quad (37)$$

Where  $k_x$  and  $k_y$  are heat conduction coefficients in x and y directions, and  $C$  is the heat capacity.

Extend the convection term in Eq. (37) to a second-order derivative term with pressure, that is:

$$-v_x \frac{\partial T}{\partial x} - v_y \frac{\partial T}{\partial y} = -\frac{\partial T v_x}{\partial x} - \frac{\partial T v_y}{\partial y} = \nabla \cdot \left( T \frac{k}{\mu} \nabla p \right) \quad (38)$$

Thus, the convection-diffusion equation in Eq. (37) is extended to the heat and mass transfer coupling problem governed by Eq. (39) and Eq. (40).

$$\frac{\partial}{\partial x}\left(k_x \frac{\partial T}{\partial x}\right) + \frac{\partial}{\partial y}\left(k_y \frac{\partial T}{\partial y}\right) + \nabla \cdot \left( T \frac{k}{\mu} \nabla p \right) = C \frac{\partial T}{\partial t} \quad (39)$$

$$\frac{k}{\mu} \nabla p = (v_x, v_y) \quad (40)$$

Therefore, when node  $i$  is the central node, the discrete format of the convection term in Eq. (37) can adopt the same discrete scheme as Eq. (15), that is:

$$-v_x \frac{\partial T}{\partial x} - v_y \frac{\partial T}{\partial y} = \nabla \cdot \left( T \frac{k}{\mu} \nabla p \right) = \sum_{j=1}^{n_i} \left[ T_{ij} \frac{k_{ij}}{\mu_{ij}} (m_{3,j}^i + m_{4,j}^i) (p_{(i,j)} - p_i) \right] \quad (41)$$

The temperature value of each node can be calculated by using the sequential coupling solution of Eqs. (39) and (40) in this paper. The high-accuracy results shown in examples 1 and 2 illustrate the feasibility of this method. For example, it can be seen from Section 3.1 that for a convection-diffusion equation shown in Eq. (30), the equation can be extended to the coupled heat and mass transfer problem in Eqs. (27) and (28), so the presented upwind GFDM can be used to obtain the high-accuracy solution of the convection-diffusion equation.

## 4. Conclusions and future work

This paper presents an analysis method of heat and mass transfer coupled model in porous formation based on meshless GFDM, which provides an effective new technology for clean geothermal resource development

and oil and gas reservoir thermal recovery. This method describes the physical domain by allocating nodes rather than dividing grids, and gives the upwind scheme of physical parameters without modifying the node influence domain and the treatment method of heterogeneous physical parameters when the explicit function form of physical parameters is unknown, forming the upwind GFDM for single-phase heat and mass transfer. Moreover, upwind GFDM also realizes high-accuracy numerical calculation of convection-diffusion equation.

Compared with the traditional mesh-based methods, this method uses meshless nodes to describe the computing domain, avoids the difficulty of high-quality mesh generation in the computing domain, and has the advantages of more flexibility and simplicity in dealing with the computing domain with complex geometric. The numerical examples in this paper also prove that the presented upwind GFDM has higher calculation accuracy than FEM in the region with significant temperature change.

Although the method in this paper only focuses on the modeling of single-phase heat and mass coupled problem, it gives the GFDM-based upwind scheme of physical parameters in multi-physics coupling problem and the treatment method of heterogeneity of physical parameters only based on node physical parameter values, without the specific function form of heterogeneous physical parameters, and the specific function expression of heterogeneous physical parameters of the underground reservoir is generally indeed unknown. Therefore, the upwind GFDM in this paper is expected to provide an important reference for the application of GFDM in multi-physics coupling modeling, multiphase flow and compositional flow model, etc.), promote the application and popularization of GFDM in complex physical problems, and further verify whether various treatment methods of physical parameters in this study of upwind GFDM based multi-physics coupling analysis are reasonable.

## 5. Acknowledgements

Dr. Rao thanks the supports from the National Natural Science Foundation of China (Grant Nos. 52104017, 51874044, 51922007), and the open fund of the National Oil Shale Exploitation R & D Center of China (Grant No. 33550000-21-ZC0611-0008), and the open fund of Cooperative Innovation Center of Unconventional Oil and Gas (Ministry of Education & Hubei Province, Yangtze University) (Grant No. UOG2020-17).

## 7. References

- [1] Bear, J., and Y. Bachmat. "Introduction to Modeling of Transport Phenomena in Porous Media." theory & applications of transport in porous media (1990).
- [2] Zhou, J., Y. Zhang, and J. K. Chen. "Numerical simulation of compressible gas flow and heat transfer in a microchannel surrounded by solid media." *International Journal of Heat and Fluid Flow* 28.6(2007):1484-1491.
- [3] Lewis, R. W., P. J. Roberts, and B. A. Schrefler. "Finite element modelling of two-phase heat and fluid flow in deforming porous media." *Transport in Porous Media* 4.4(1989):319-334.
- [4] Wu, Y. S., and K. Pruess. "Numerical simulation of non-isothermal multiphase tracer transport in heterogeneous fractured porous media." *Advances in Water Resources* 23.7(2000):699-723.
- [5] H. Class, R. Helmig, P. Bastian. Numerical simulation of non-isothermal multiphase multicomponent processes in porous media.: I. An efficient solution technique[J]. *Advances in water resources*, 2002, 25:533-550.
- [6] J.J. Benito, F. Urena, L. Gavete, Influence of several factors in the generalized finite difference method, *Appl. Math. Model.* 25 (12) (2001) 1039–1053.
- [7] J.J. Benito, F. Urena, L. Gavete, R. Alvarez, An h-adaptive method in the generalized finite differences, *Comput. Methods Appl. Mech. Engrg.* 192 (5–6) (2003) 735–759.
- [8] Y. Gu, W. Qu, W. Chen, L. Song, C. Zhang, The generalized finite difference method for long-time dynamic modeling of three-dimensional coupled thermoelasticity problems, *J. Comput. Phys.* 384 (2019) 42–59.
- [9] H Xia, and Y. Gu . "Generalized finite difference method for electroelastic analysis of three-dimensional piezoelectric structures." *Applied Mathematics Letters* 117.2(2021):107084.
- [10] H. Xia, Y. Gu, Short communication: The generalized finite difference method for electroelastic analysis of 2D piezoelectric structures, *Eng. Anal. Bound. Elem.* 124 (2021) 82–86.
- [11] Urena F, Salet E, Benito J J, et al. Solving third- and fourth-order partial differential equations using GFDM: application to solve problems of plates[J]. *International Journal of Computer Mathematics*, 2012, 89(3): 366-376.

- [12] P.-W. Li, C.-M. Fan, Generalized finite difference method for two-dimensional shallow water equations, *Eng. Anal. Bound. Elem.* 80 (2017) 58–71.
- [13] W. Qu, H. He, A spatial–temporal GFDM with an additional condition for transient heat conduction analysis of FGMs, *Appl. Math. Lett.* 110 (2020) 106579.
- [14] J.J. Benito, F. Ureña, L. Gavete, E. Salet, M. Ureña, Implementations with generalized finite differences of the displacements and velocity-stress formulations of seismic wave propagation problem, *Appl. Math. Model.* 52 (2017) 1–14.
- [15] Y. Wang, Y. Gu, C.-M. Fan, W. Chen, C. Zhang, Domain-decomposition generalized finite difference method for stress analysis in multi-layered elastic materials, *Eng. Anal. Bound. Elem.* 94 (2018) 94–102.
- [16] C.M. Fan, P.W. Li, Generalized finite difference method for solving two-dimensional Burgers' equations, *Proc. Eng.* 79 (2014) 55–60.
- [17] P.-W. Li, Space–time generalized finite difference nonlinear model for solving unsteady Burgers' equations, *Appl. Math. Lett.* 114 (2021) 106896.
- [18] Z.-J. Fu, Z.-Y. Xie, S.-Y. Ji, C.-C. Tsai, A.-L. Li, Meshless generalized finite difference method for water wave interactions with multiple-bottom-seated-cylinder-array structures, *Ocean Eng.* 195 (2020) 106736.
- [19] Gu Yan, Wang Lei, Chen Wen, et al. Application of the meshless generalized finite difference method to inverse heat source problems[J]. *International Journal of Heat and Mass Transfer*, 2017, 108(A): 721-729.
- [20] Z.-J. Fu, Z.-C. Tang, H.-T. Zhao, P.-W. Li, T. Rabczuk, Numerical solutions of the coupled unsteady nonlinear convection–diffusion equations based on generalized finite difference method, *Eur. Phys. J. Plus* 134 (6) (2019) 272.
- [21] Gu Y, Sun HG. A meshless method for solving three-dimensional time fractional diffusion equation with variable-order derivatives. *Applied Mathematical Modelling*, 2020, 78: 539-549
- [22] Syc, A, A. Kch, and B. Cmf. "Improvement of generalized finite difference method for stochastic subsurface flow modeling - ScienceDirect." *Journal of Computational Physics* (2020).
- [23] Gavete L, Gavete M L, Benito J J. Improvements of generalized finite difference method and comparison with other meshless method[J]. *Applied Mathematical Modelling*, 2003, 27(10): 831-847.
- [24] Noorish Ad, J., & Mehran, M. (1982). An upstream finite element method for solution of transient transport equation in fractured porous media. *Water Resources Research*, 18(3), 588-596.
- [25] Leer, B. V.. "Towards the ultimate conservative difference scheme III. Upstream-centered finite-difference schemes for ideal compressible flow - ScienceDirect." *Journal of Computational Physics* 23.3(1977):263-275.
- [26] Dja De L, K., and S. Nicaise. "A non-conforming finite volume element method of weighted upstream type for the two-dimensional stationary Navier-Stokes system." *Applied Numerical Mathematics* 58.5(2008):615-634.
- [27] Atluri, S. N., and S. Shen. "The Meshless Local Petrov-Galerkin (MLPG) Method: A Simple & Less-costly Alternative to the Finite Element and Boundary Element Methods." *Computer Modeling in Engineering and Sciences* 3.1(2002).
- [28] Cheng, M., and G. R. Liu. "A novel finite point method for flow simulation." *International Journal for Numerical Methods in Fluids* 39.12(2002):1161-1178.